

Full length article

High linearity temperature-compensated SPR fiber sensor for the detection of glucose solution concentrations

Yao Xu^a, Jianhua Chang^{a,b,*}, Haibin Ni^{a,b}, Tengfei Dai^a, Alexey V. Krasavin^c, Ming Chen^a

^a School of Electronics and Information Technology, Nanjing University of Information Science and Technology, Nanjing 210044, China

^b Jiangsu Collaborative Innovation Center of Atmospheric Environment and Equipment Technology (CICAET), Nanjing University of Information Science & Technology, Nanjing 210044, China

^c Department of Physics and London Centre for Nanotechnology, King's College London, Strand, London WC2R 2LS, UK

ARTICLE INFO

Keywords:

Sensor
Optical fiber
Surface plasmon resonance
Temperature compensation.)

ABSTRACT

In the realm of optical fiber sensing, conventional surface plasmon resonance (SPR) sensors often face challenges due to their low linearity, broad resonance, and susceptibility to external temperature changes. To that end, we evaluate a groundbreaking approach with a temperature-compensating SPR biosensor based on the Mach-Zehnder interferometer (MZI), featuring a novel tapered multimode fiber-single mode fiber-multimode fiber (MMF-SMF-MMF) architecture. Specifically, the SPR is excited on a silver film modified by reduced graphene oxide (rGO) and π - π stacked pyrene-1-boric acid providing specific glucose binding ability. The MZI effect compensating for ambient temperature influence on the SPR is realized with the MMF-SMF-MMF structure. The study also explores the use of Fast Fourier Transform (FFT) for separate, granular analysis of the MZI and SPR signals and improves the linearity of the sensor using a novel centroid-fitting technique. This method utilizes the shift of calculated centroid coordinates rather than the single dip resonance wavelength from SPR, enhancing the overall performance of the sensor. The experimental results demonstrate excellent glucose sensitivity of 2.819 nm/mM, a linear range of 0–10 mmol/L, a LOD of 0.12 mM/L and concurrent temperature compensation. Compact and easy to fabricate, the proposed SPR sensor provides a novel solution for accurate glucose concentration detection in human blood.

1. Introduction

Glucose is a vital component of human blood [1] and an essential biomarker for medical diagnosis and treatment [2]. Low blood sugar levels can induce symptoms such as dizziness, fatigue, lack of focus, anxiety, and nausea. Severe hypoglycemia may lead to convulsions and coma, even posing a life-threatening risk. Conversely, elevated blood sugar levels also negatively affect the kidneys, eyes, nervous and immune systems, also causing cardiovascular diseases, heart disease and stroke risk. Therefore, monitoring blood glucose levels has a prime importance. The conventional method for detecting blood glucose concentration, the glucose oxygen electrode method [3], has limited accuracy owing to factors such as small generated current, interference from human bioelectricity, and temperature sensitivity. Although the glucose sensor based on spectrophotometry has a wide monitoring range, its application is limited due to its complex manufacturing process, high cost, cumbersome operation, and susceptibility to interference from

compounds [4]. Therefore, alternative measurement methods that are simple, fast, highly accurate, and have strong anti-interference ability are crucial for accurate monitoring of glucose concentration, particularly in patients with diabetes. The proposed optical fiber surface plasmon resonance (SPR) sensor is a promising alternative to conventional glucose-monitoring methods [5–7]. Its passive detection feature provides strong anti-electromagnetic interference ability [8], while the use of resonance peak drift measurements ensures high stability [9]. The compactness and integration ability of the optical fiber enables its insertion into subcutaneous tissues [10], providing real-time and accurate glucose concentration values.

However, the sensitivity and accuracy of optical fiber SPR sensors require further improvement compared with traditional prism-model SPR sensors based on angle detection [11]. Temperature changes can also alter the refractive index of the tested material and hence affect the test results [12]. Therefore, the fiber SPR sensors are often equipped with Bragg gratings or Fabry-Perot multimode interferometers to

* Corresponding author at: School of Electronics and Information Technology, Nanjing University of Information Science and Technology, Nanjing 210044, China.
E-mail address: jianhuachang@nuist.edu.cn (J. Chang).

compensate for the temperature drift in the SPR spectrum [13,14]. However, the implementation of these methods increases the sensor size, complicates its structure, and weakens the inherent advantages of fiber-optic sensors. At the same time, current research focuses on introducing two-dimensional materials such as graphene [15] or metal nanoparticles [16] onto a metal film to enhance the sensitivity of the sensor owing to their excellent electrical and optical properties. Graphene and related materials possess high carrier mobility that promotes electron transfer to the metal film of an SPR sensor [17]. This leads to stronger coupling at the interface and enhances surface electric field, thereby increasing the sensitivity of the sensor. Additionally, graphene oxide exhibits good biological affinity, which promotes the adsorption of biological molecules onto the metal membrane of the SPR sensor [18] and further improving its sensitivity for detecting biological molecules [19]. Reduced graphene oxide (rGO), a member of the graphene family, possesses the advantages of both graphene and graphene oxide [20]. In addition to its high carrier mobility, rich surface functional groups and strong hydrophilicity make it easy for rGO to connect to the biosensor membrane and measured substance. Therefore, it has broad applications in SPR sensors. Kant et al. proposed an optical fiber SPR sensor based on a combination of rGO and chitosan-modified silica sol gel to detect caffeine concentration [21]. Semwal et al. proposed a type of SPR sensor based on a coreless optical fiber coated with a composite film of rGO and polyaniline on its surfacet to detect the external pH value [22]. However, adding the rGO significantly widened the resonance of the sensor, which affected its accuracy. Simultaneously, the multimode regime in the optical fiber leads to different incident angles. Each of these angles produces different resonance wavelengths [23] and the transmission spectrum resonance of the optical fiber structure is also widened compared to the relatively mature prism counterpart [24].

In this study, we present an optical fiber sensor that simultaneously employs SPR and Mach-Zehnder interferometer (MZI) effects, provides high detection sensitivity for glucose concentration and enables real-time monitoring of the ambient environmental temperature. Additionally, the linearity and detection resolution of the sensor is improved by employing the centroid-fitting method, which uses the centroid coordinates as a sensing monitoring parameter instead of the shift in the resonance wavelength from a single dip of the SPR. Compared to traditional optical fiber SPR sensors [25], the proposed sensor exhibits superior performance in terms of sensitivity, accuracy, and linearity for glucose concentration detection, offering significant advantages over conventional sensing methods.

2. Fabrication and principle

2.1. Materials and methods

The fiber sensor developed in this work was fabricated from a multimode fiber (MMF, 62.5/125 μm , Changfei company, China) and a SMF single-mode fiber (SMF, 8.2/125 μm , Changfei company, China). The instrument used for tapering is fusion splicer (FSM-60, Fujikura inc., Japan) which performs precise fusion splicing of optical fibers, ensuring connection quality and stability. Fiber optic fusion splicers align and connect optical fibers by utilizing the internal microprocessor and electrode discharge which greatly saves time and enhances repeatability. Fusion splicing of different types of optical fibers requires different settings, including discharge power, discharge time, overlap distance, and alignment angle, among other important parameters. All these parameters are determined through multiple experiments until the fiber loss reaches the minimum. Magnetron sputtering coating machine (JSD350, Weina company, China) works on the principle of using a magnetic field to create plasma, which bombards a target material, causing its atoms to be ejected and deposited onto the surface of the sensor, forming a metal film. The control of the sputtering time, current intensity, vacuum level, and other parameters allows regulating the thickness and smoothness of the metal film. Fig. 1 illustrates the process adopted for fabricating the proposed SPR sensor. First, the multimode fiber (MMF, 62.5/125 μm) and SMF single-mode fiber (SMF, 8.2/125 μm) were cut flat using a fiber-cutting tool, followed by fusion splicing using a fusion splicer (FSM-60). Next, the sensing unit was cut to the desired length, and the MMF was fused to the other end of the SMF while reserving 1.5 cm, overall resulting in an MMF-SMF-MMF structure. A 37.6 % volume fraction HF solution (purchased from Aladdin Biochemical Technology) was dropped onto the surface of the middle 0.5 cm of the SMF, which was then corroded over 40 min to form a tapered structure as the HF diffused to both ends with time. After etching, the residual HF on the fiber surface was rinsed with deionized water. The SMF surface was wiped with anhydrous ethanol and dried with nitrogen gas. The processed fiber was then fixed on a glass slide and placed in a magnetron sputtering coating machine (JSD350) to deposit a 50 nm-thick silver film. The magnetron sputtering current was maintained at 30 mA, and the deposition time was set to 150 s. The proposed SPR sensor fabrication method is simple, feasible, and easy to implement.

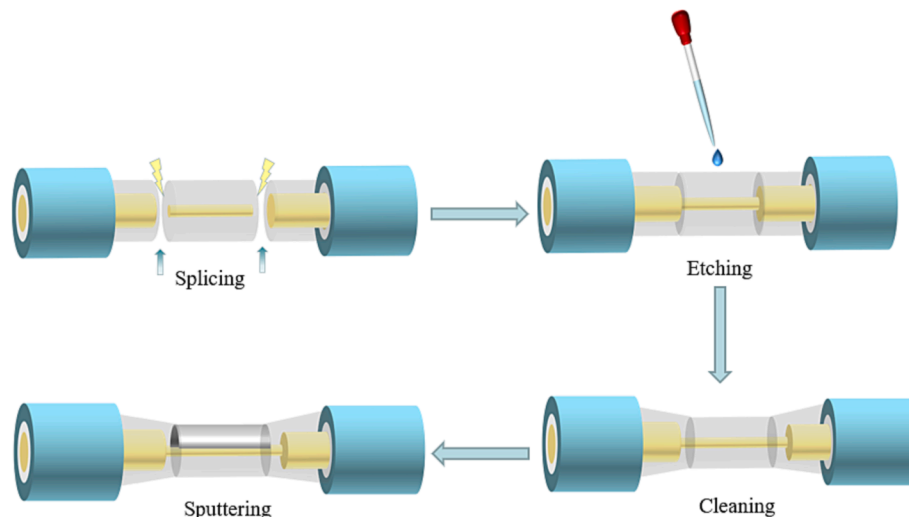


Fig. 1. Fabrication process for the optical fiber sensor.

2.2. Sensor design and principles analysis

Fig. 2 shows the sensing structure, which uses a small segment of an SMF sandwiched between two MMFs. The middle part of the SMF is immersed in HF acid, which spreads to both sides of the SMF over time and causes the formation of a tapered structure due to uneven corrosion [26]. A 50 nm-thick silver film is deposited on the surface of the SMF to enhance the interaction of evanescent waves (EWs) with the surrounding medium, while eliminating the influence of multimode interference on the cladding through acid etching. When light is introduced from the MMF into the SMF, it excites higher-order cladding modes that propagate in the cladding of the SMF whereas the fundamental mode continues to propagate in the core. Conversely, when light enters the MMF from the SMF, the MZI effect occurs between the two excited modes. Simultaneously, surface plasmon waves (SPW) are excited on the silver film surface.

For SPR, total internal reflection occurs when the light propagates in the cladding of the SMF and reaches the interface between the optical fiber and the silver film. Consequently, a portion of the energy enters the metal layer in the form of EWs. The incident wave vector of the EWs can be expressed as follows:

$$K_z = \frac{\omega}{c} \sqrt{\varepsilon_c} \sin\theta \quad (1)$$

The propagation constant of the SPW of the metal can be expressed as:

$$K_{spw} = \frac{\omega}{c} \sqrt{\frac{\varepsilon_1 \varepsilon_2}{\varepsilon_1 + \varepsilon_2}} \quad (2)$$

where θ is the angle of incidence of light; c is the speed of light in vacuum; ω is the angular frequency of the incident light; and $\varepsilon_c, \varepsilon_1$, and ε_2 are the dielectric constants of the optical fiber cladding, metal layer, and surrounding dielectric layer, respectively. The propagation constant of the evanescent wave is equal to that of the SPW. Thus:

$$\frac{\omega}{c} \sqrt{\frac{\varepsilon_1 \varepsilon_2}{\varepsilon_1 + \varepsilon_2}} = \frac{\omega}{c} \sqrt{\varepsilon_c} \sin\theta \quad (3)$$

Resonance occurs when the EWs match the resonance frequency of the SPWs at the interface between the fiber and the silver film [27]. The energy of the incident light wave is resonantly transformed into the oscillation energy of the plasma wave, resulting in reduced reflected light and a resonance absorption peak in the resulting spectrum.

For the MZI, a two-mode interference model is used to analyze the transmission spectrum [28]. The output intensity of the sensor is given by

$$I = I_{\text{core}} + I_{\text{cladding}} + \sqrt{I_{\text{core}} I_{\text{cladding}}} \cos\Delta\varphi \quad (4)$$

where I_{core} and I_{cladding} represent the intensities of the core and cladding modes, respectively. λ and $\Delta\varphi$ represent the wavelength of the input light and phase difference between the two modes, respectively. $\Delta\varphi$ can be expressed as [29]

$$\Delta\varphi = \frac{2\pi L_{SMF}}{\lambda} (n_{\text{neff}}^{\text{core}} - n_{\text{neff}}^{\text{cladding}}) \quad (5)$$

where L_{SMF} is the length of the SMF, while $n_{\text{neff}}^{\text{core}}$ and $n_{\text{neff}}^{\text{cladding}}$ are the effective refractive indexes (RIs) of the core and the cladding modes, respectively. According to the interference theory, the wavelength corresponding to the interference extremum λ_m given by:

$$\lambda_m = \frac{4\pi \Delta n_{\text{eff}}^m L}{2(N+1)\pi} \quad (6)$$

In the equation, N is an integer. It can be observed that changes in the refractive index of the environment lead to the variation in the effective refractive index, while the temperature causes changes in L , resulting in a drift of the interference dips.

2.3. Functional modification of the sensor

The surfaces of the optical fibers were functionalized before measuring the glucose concentration. Fig. 3 illustrates the process of modifying the silver-plated sensor using rGO (purchased from Nanjingxianfeng Nanomaterials) and PBA (purchased from Aladdin Biochemical Technology). First, the silver-plated sensor was cleaned with acetone solution, washed with deionized water to remove any remaining solution, and dried with nitrogen. The fiber sensor was immersed in a 1 mg/mL poly diallyl dimethylammonium chloride (PDDA) solution for 1 h. PDDA is a polymer electrolyte that becomes ionized when dissolved in water, leaving behind positively charged polymer chains. When the polymer attaches to the fiber surface, the surface of the Ag film can acquire a positive charge. In the second step, the rGO nanoslices were deposited on the surface of the optical fibers using the pull method. Reduced graphene oxide disulfide nanosheet dispersion (0.5 mg/mL) was purchased from Nanjingxianfeng Nanomaterials. The rGO solution is sonicated in an ultrasonic machine for thirty minutes to ensure its uniform dispersion. After rinsing off the excess PDDA solution from the sensor surface with deionized water, the optical fiber was immersed in a 0.5 mg/ml single-layer rGO dispersion for two minutes. This step was repeated 10 times. The sensor was dried on a heating plate at 70 °C to remove any remaining water, after which the negatively charged rGO was fixed on the surface of the positively charged silver film by the adsorption between positive and negative charges. Fig. 4(a) shows the scanning electron microscopic (SEM) image of the rGO. It can be seen from the SEM that rGO has a very large specific surface area and many wrinkles, which are conducive to the adsorption of PBA. Fig. 4(b) shows the Raman spectrum of rGO with two bands at 1340 and 1583 cm^{-1} , known as the D and G bands, respectively. This confirms the successful attachment of rGO to the surface of the optical fiber. In the third step, PBA (10 mg) was dissolved in deionized water (10 mL), then the rGO-modified sensor was immersed in a 1 mg/mL PBA solution for eight hours, creating π - π interactions to fix the PBA onto the rGO nanosheets [30]. The sensor was washed with acetone and deionized water to remove the unbonded PBA. The resulting functionalized sensor is suitable for measuring glucose concentrations because reduced

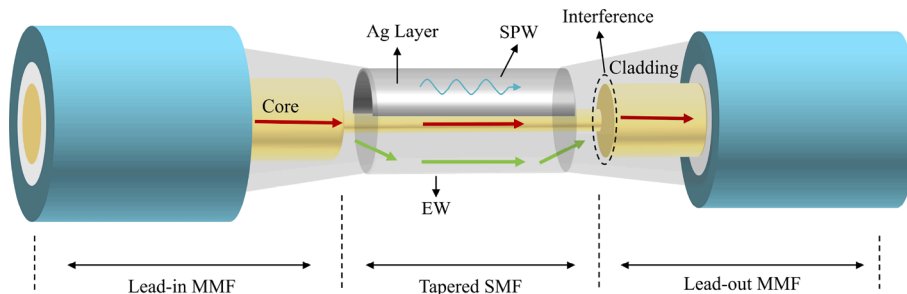


Fig. 2. Schematic of the optical fiber sensor.

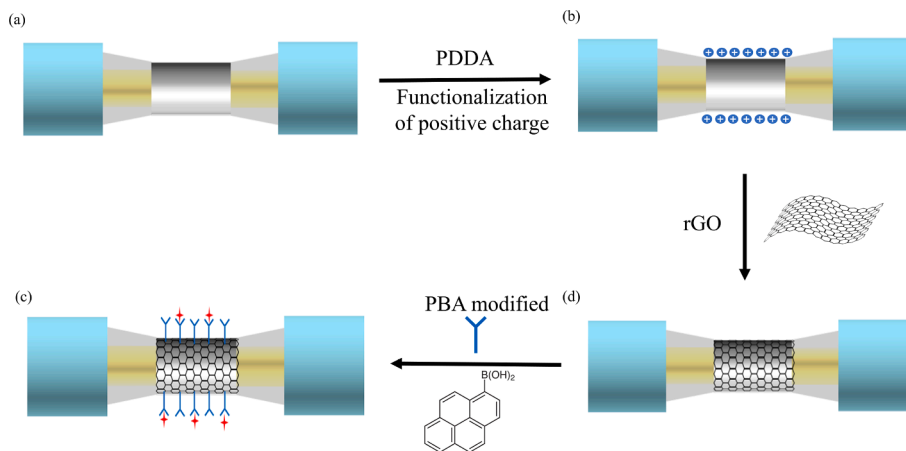


Fig. 3. Functionalization process of the SPR glucose sensor.

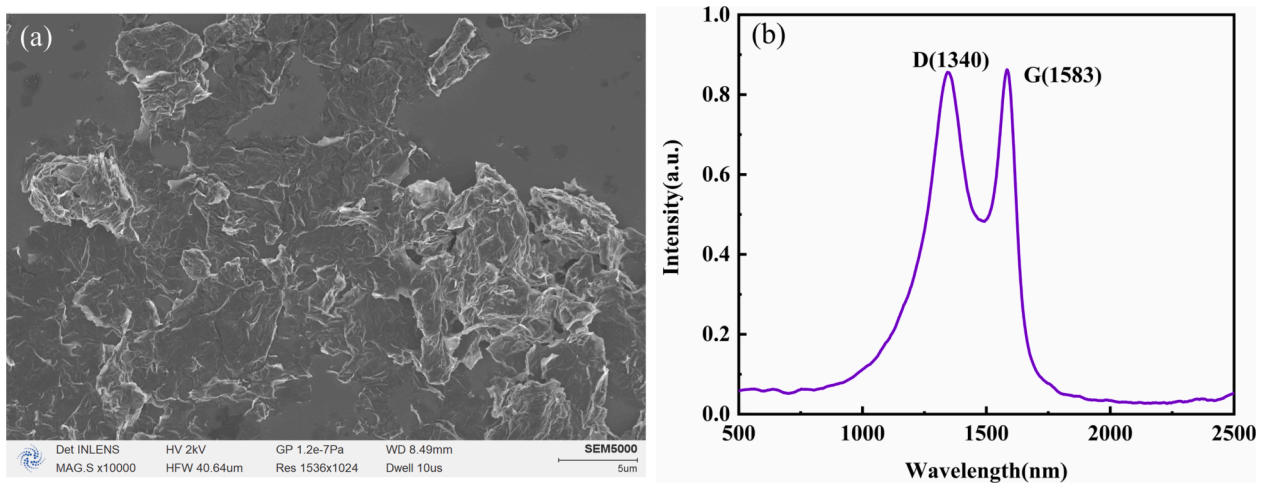


Fig. 4. (a) SEM image and (b) Raman spectra of rGO.

graphene oxide exhibits strong affinity to immobilize a large amount of PBA on its surface and PBA could form reversible covalent bonds with glucose molecules containing diol units, enabling the sensor to dynamically adsorb glucose molecules and achieve selective detection of glucose.

2.4. Demodulation and optimization of the sensor

The sensor output signal simultaneously contains the SPR and MZI effects, resulting in a superimposed spectrum, as shown in Fig. 5 (a). Fast Fourier transform (FFT) was performed to separate the SPR and MZI signals from the original spectrum [31]. The spatial frequency spectrum at a refractive index of 1.333 is shown in Fig. 5(b), where the primary peak (Peak SPR) originates from the SPR absorption peak, while the weaker peak is caused by the MZI. The SPR and MZI signals were separated using a bandpass filter, as shown in Fig. 5 (c) and (d), respectively. The spatial frequency components of the separated SPR and MZI signals underwent inverse Fourier transform to generate separate SPR and MZI wavelength spectrograms. Thus, the SPR and MZI signals in the original spectra were effectively separated and further processed individually. Additionally, the noise, i.e. spacial components other than the SPR and MZI signals, was filtered out. Therefore, the sensor is less susceptible to noise interference, which leads to a good signal-to-noise ratio. The results demonstrated the success of the method for separating these two signals in the original spectrum, enabling a more accurate analysis of the individual SPR and MZI effects.

Distinct from traditional prism-based SPR sensors, optical fibers have multiple light propagation angles and each angle has a unique SPR resonance wavelength, which widens resonance in the transmission spectrum. Modifying the fiber surface with rGO improves the sensitivity, but further widens the spectral features, which can adversely affect the sensor performance by reducing the accuracy and linearity. Consequently, the prism's method of utilizing the dip of the resonance offers a limited means of analysis in the case of the fiber, resulting in diminished linearity. To address this issue, we propose using the centroid coordinates as the sensing parameter. Centroid fitting method features fitting the SPR curve with a mathematical function, choosing the inflection point to mark the baseline, and establishing the centroid coordinates within the region enclosed by the baseline and the fitting function as the sensing parameter describing the resonance position. Therefore, this method could facilitate a thorough analysis of the complete resonance profile to improve the sensor's linearity. The proposed approach is shown in Fig. 6. The measured discrete spectral data of the separated SPR signal were fitted by a Gaussian function using a Gaussian curve fitting algorithm.

$$T_{gauss} = T_0 \exp \left[-\frac{(\lambda - \lambda_c)^2}{2 \cdot FWHM^2} \right] \quad (7)$$

Here, λ_c is the resonance wavelength, T_0 is the transmittance corresponding to it and FWHM is the full width at half maximum of the resonance. The y-coordinate of the inflection point a of the fitted Gaussian

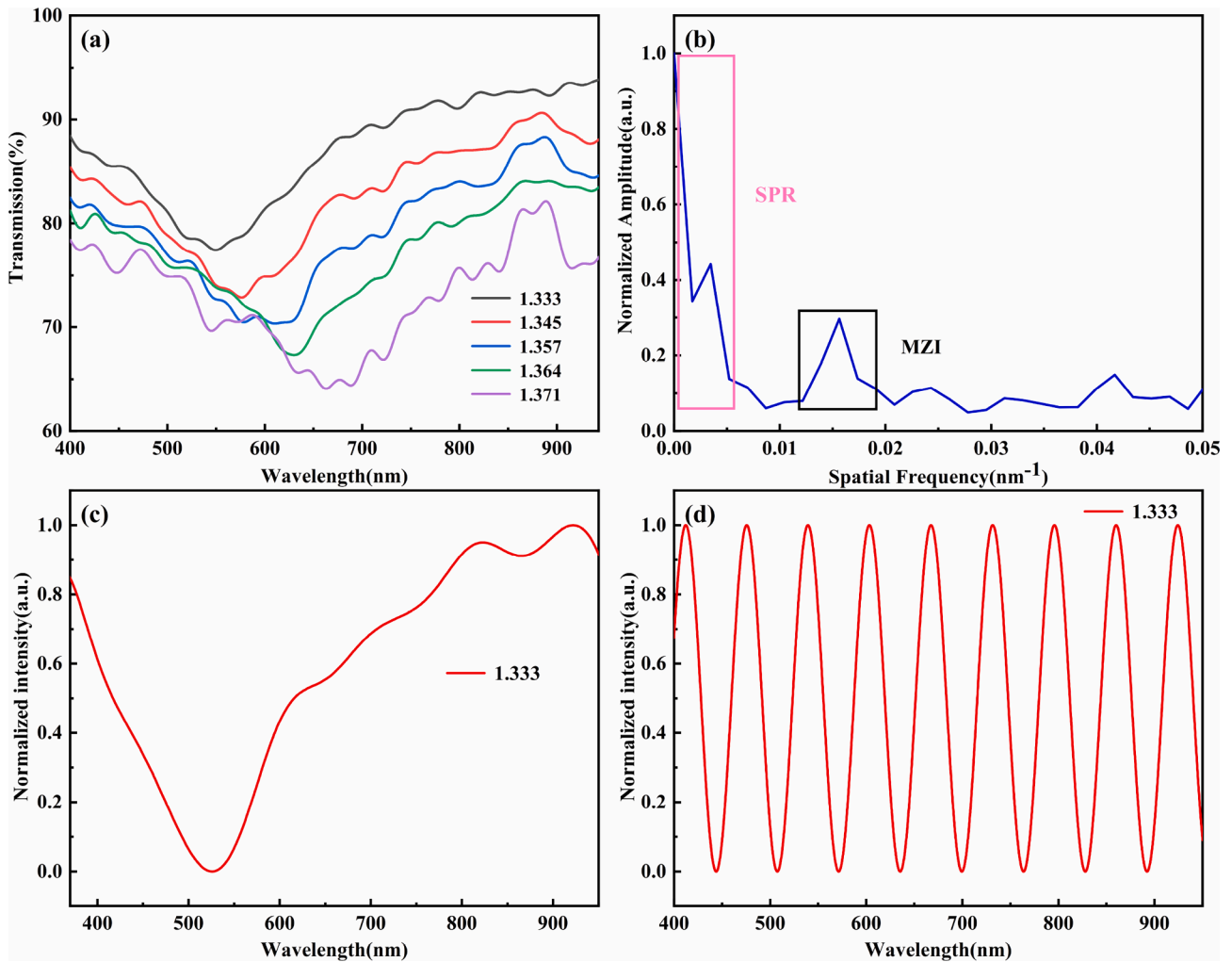


Fig. 5. (a) Original spectra. (b) Spatial frequency distribution after FFT in 1.333 RIU. (c) SPR spectrum in 1.333 RIU after band pass filtering. (d) MZI spectrum in 1.333 RIU after band pass filtering.

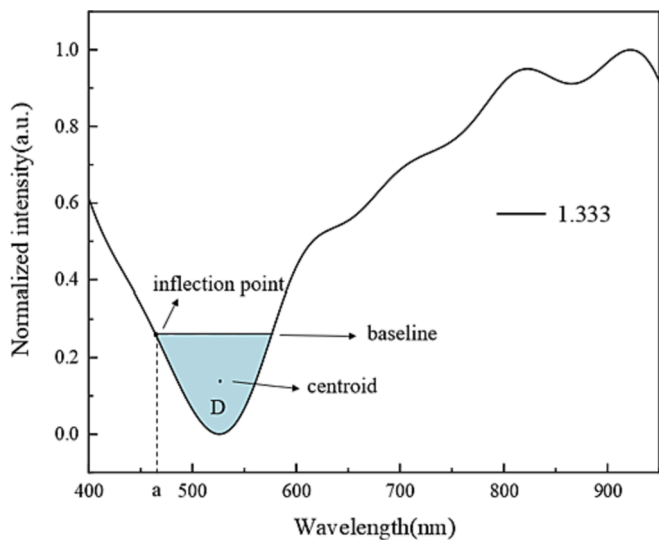


Fig. 6. Principle of the centroid-fitting algorithm.

function was used to define the baseline:

$$\left| \frac{dT_{gauss}}{d\lambda} \right|_a = \max \left(\left| \frac{dT_{gauss}}{d\lambda} \right| \right) \quad (8)$$

$$y_{base} = T_{gauss}(a) \quad (9)$$

Using Eqn 10, the centroid wavelength of the area D enclosed by the baseline and the fitted Gaussian function was calculated.

$$\bar{\lambda} = \frac{\iint_D \lambda T_{gauss} d\sigma}{\iint_D T_{gauss} d\sigma} \quad (10)$$

It was used to define the positions of the resonances for further calculations of the spectral shifts.

3. Results and discussion

3.1. Experimental setup

The experimental setup, which is shown in Fig. 7, comprises a broadband light source (Ocean Insight, HP-2000LL, 400–2500 nm), a spectrometer (Ocean Optics HR2000 + ES) and the optical fiber sensor. The light passed through the sensor and was recorded by the spectrometer, capturing the simultaneous SPR and MZI transmission spectra. The measured spectra were stored and processed using the centroid-

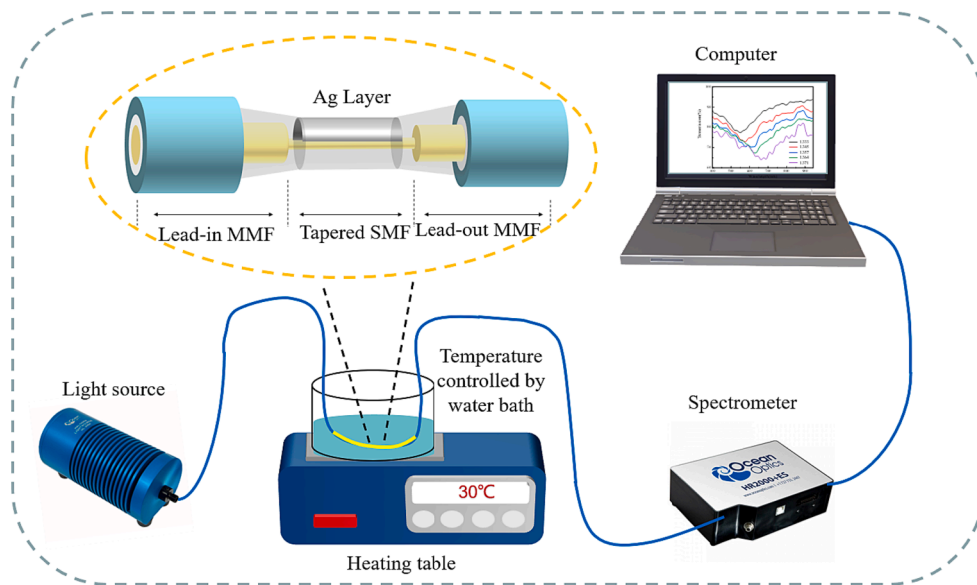


Fig. 7. Structure of the experimental device.

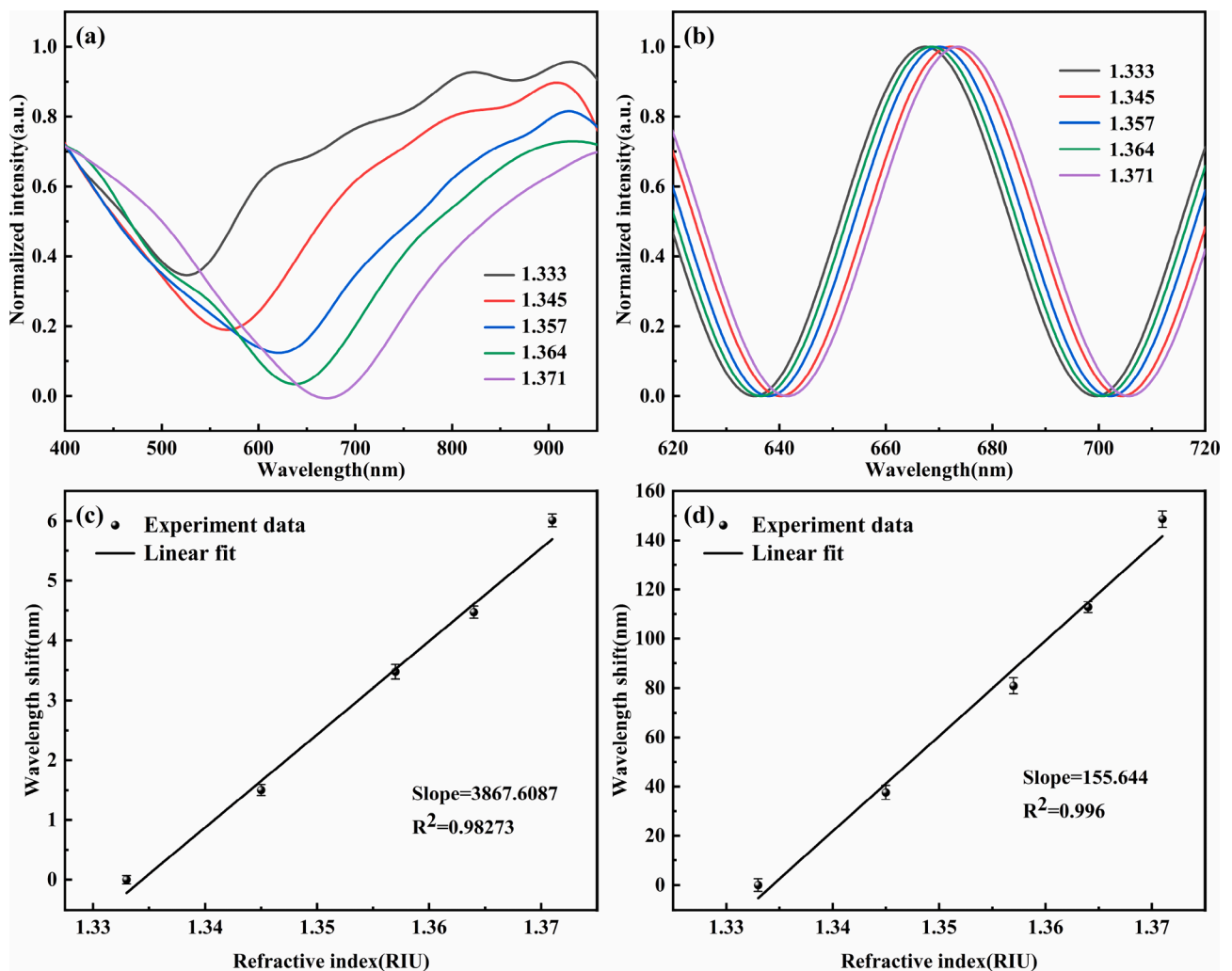


Fig. 8. RI responses of the (a) SPR and (b) MZI signals at a constant T of 30 °C. Linear fit of (c) SPR and (d) MZI resonance wavelength in the studied RI range.

fitting algorithm to improve the accuracy of the sensor readings. A bath containing the analyzed solution (glycerol in water) and the sensor was placed on a small heating plate. The temperature was adjusted by controlling the heating plate, while different concentrations of glycerol in water were used to vary the refractive index of the solution. After a single data collection cycle, the sensor was cleaned with deionized water until it returned to its initial state. The average of three measurements was used as the reference data.

3.2. RI and temperature sensing characteristics

The RI and temperature-sensing characteristics of the sensor must be assessed before testing the glucose parameters. The RI sensing performance was evaluated by immersing the sensor in glycerol solutions at 30 °C, with RIs of 1.333, 1.345, 1.357, 1.364, and 1.371. To obtain accurate readings, the original spectrum underwent FFT, and the SPR and MZI spectra were separated using a bandpass filter for normalization, as shown in Fig. 8(a) and 8(b), respectively. As the RI increased, the resonance peak red-shifted from 518.67 nm to 667.27 nm. Additionally, as the external refractive index increased, the interference wavelength of MZI underwent a red-shift from 635.19 nm to 641.2 nm. The SPR spectrum had a lower R-square value than the MZI spectrum owing to the adverse effects of multiple angles of light propagation in the optical fibers. The average sensitivity of the SPR spectrum was 3867.6087 nm/RIU and the regression coefficient R-square was 0.98273, while the MZI

spectrum had an average sensitivity of 155.644 nm/RIU, with a higher R-square value of 0.994, as shown in Fig. 8(c) and 8(d), respectively.

The transmission spectrum can be further affected by changes in the refractive index of the optical fiber [32], dielectric constant of the metal-plated surface [33], and RI of the external solution owing to temperature changes [34]. To reduce errors caused by temperature changes, we analyzed the temperature-sensing performance of the sensor. The sensor was immersed in deionized water, and the temperature of the heating table set to 30, 40, 50, 60, and 70 °C. The transmission spectra were recorded after the temperature stabilized. The SPR and MZI spectra were separated using FFT, as shown in Fig. 9(a) and 9(b), respectively. As the temperature increased, the SPR resonance wavelength underwent a blue shift from 518.62 nm to 513.04 nm, while the interference fringes of MZI red-shifted from 641.48 nm to 655.66 nm. The linear fitting results of the SPR and MZI are shown in Fig. 9(c) and 9(d), respectively. The temperature sensitivity of SPR was -0.134 nm/°C with an R-square of 0.983, and MZI had a sensitivity of 0.331 nm/°C with an R-square of 0.996. The RI sensing results indicated that the linearity of the SPR spectrum was lower than that of the MZI spectrum.

3.3. Optimization and temperature-compensation of the sensor

As described above, the centroid-fitting method was used to enhance the accuracy of the sensor by processing the SPR signal. We extracted the SPR spectral signal for Gaussian fitting and used the centroid

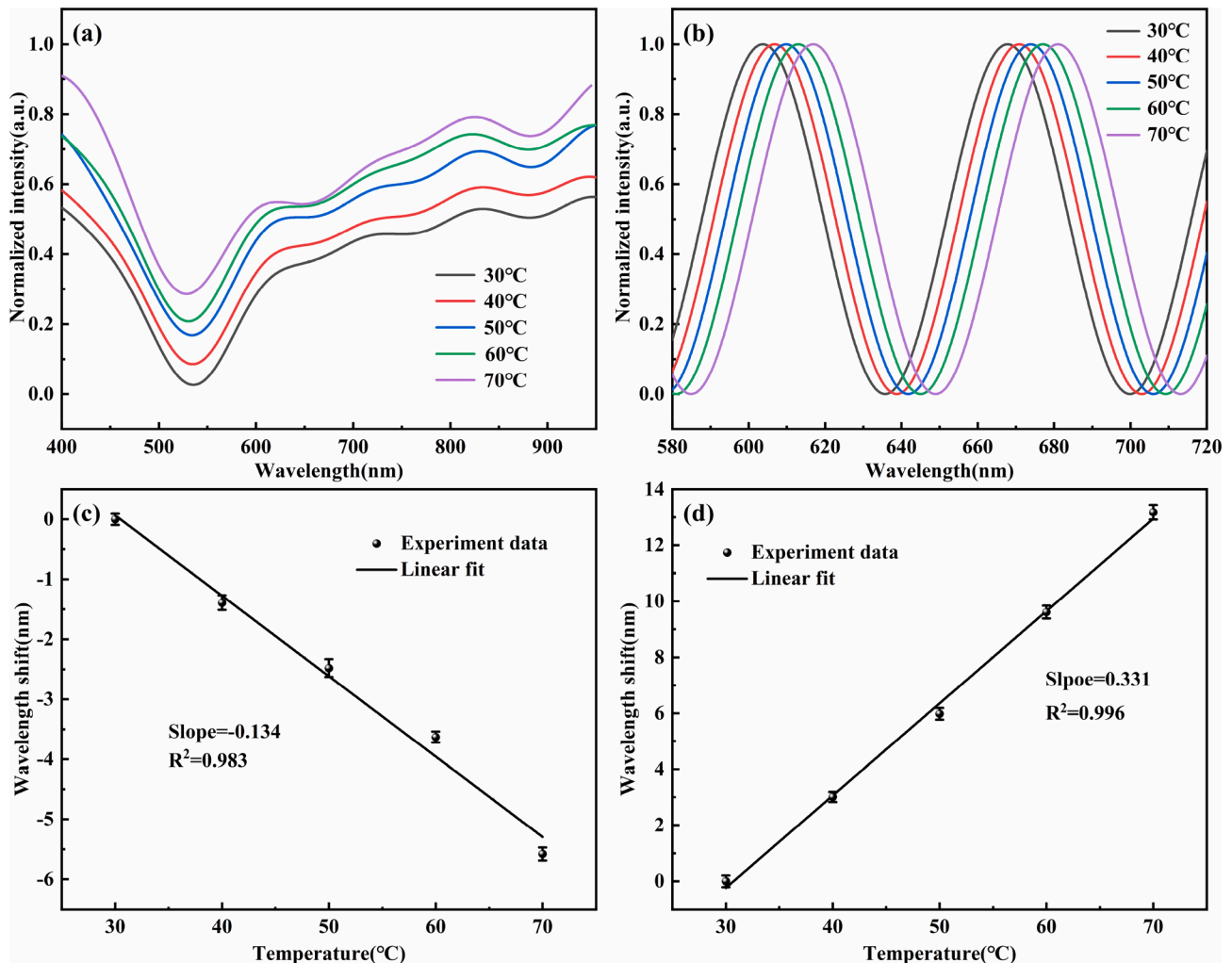


Fig. 9. Temperature responses of the (a) SPR and (b) MZI signals at a constant RI of 1.333. Linear fit of the (c) SPR and (d) MZI resonance wavelength in the studies temperature range.

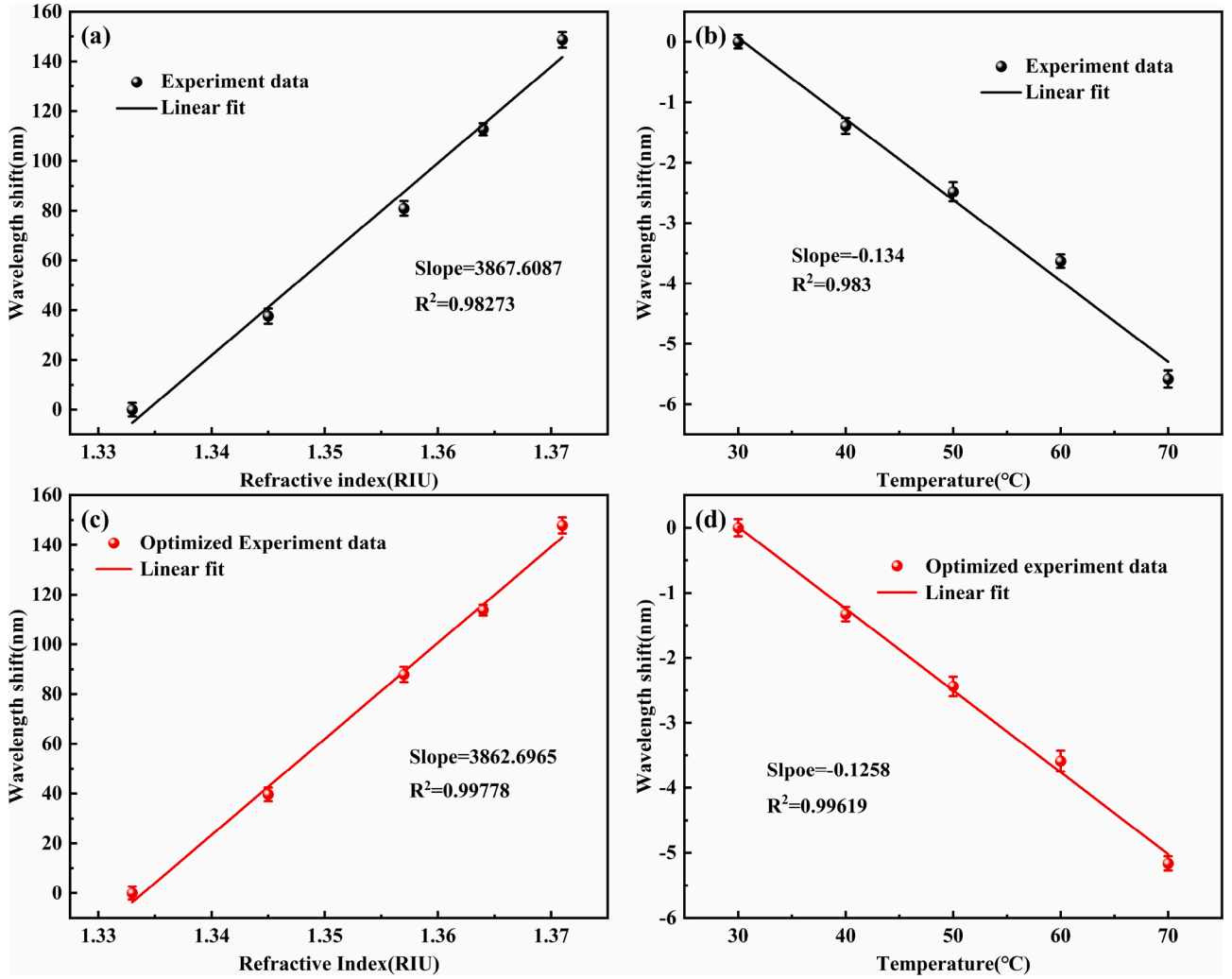


Fig. 10. Linear fit of the SPR resonance wavelength corresponding to (a) RI and (b) temperature changes. Linear fit of SPR centroid coordinates corresponding to (c) RI and (d) temperature changes.

coordinates of the area enclosed by the baseline and SPR curves to replace the traditional SPR resonance peak position as the sensing parameter. The RI and temperature linear fitting results were obtained using the resonance peak coordinates and fitted centroid coordinates as indicators, as shown in Fig. 10(a) and 10(b), and Fig. 10(c) and 10(d), respectively. The linearity of the RI and temperature improved significantly after optimization, with the R-squares of the RI linear fitting and temperature linear fitting results increasing from 0.98273 to 0.99778, and 0.983 to 0.99619, respectively.

The above discussion confirms that the MZI signal is insensitive to the variation of RI and thereby is immune to the influence of the thermal-optic coefficient. As a result, the MZI signal of the sensor provide an efficient means to avoid cross-sensitivity between RI and temperature in order to achieve temperature compensation. As the linearity of the SPR curve was optimized using centroid fitting, we could establish a sensitivity matrix to separate the RI and temperature factors. This was possible because of the significantly different sensitivities of the SPR and MZI, in respect to temperature and RI. The sensitivity matrix expressed by the following equation was used to obtain accurate and reliable readings, as demonstrated by our results.

$$\begin{bmatrix} \Delta\lambda_{SPR} \\ \Delta\lambda_{MZI} \end{bmatrix} = \begin{bmatrix} s_n^{SPR} & s_T^{SPR} \\ s_n^{MZI} & s_T^{MZI} \end{bmatrix} \begin{bmatrix} \Delta n \\ \Delta T \end{bmatrix} \quad (11)$$

Inserting experimental data into Eq. (12), Δn and ΔT can be

represented by the following matrix:

$$\begin{bmatrix} \Delta n \\ \Delta T \end{bmatrix} = \begin{bmatrix} 3862.70 & -0.12 \\ 155.644 & 0.331 \end{bmatrix}^{-1} \begin{bmatrix} \Delta\lambda_{SPR} \\ \Delta\lambda_{MZI} \end{bmatrix} \quad (12)$$

$\Delta\lambda_{SPR}$ and $\Delta\lambda_{MZI}$ represent the wavelength shifts of the SPR centroid and MZI interference fringe, respectively. s_n^{SPR} and s_n^{MZI} are the RI sensitivities of the SPR and MZI signals, respectively, while s_T^{SPR} and s_T^{MZI} represent the temperature sensitivities of the SPR and MZI signals, respectively. Δn and ΔT represent the changes in the RI and temperature detected by the sensor, respectively. Based on Eq. (12), changes in refractive index (RI) and temperature (T) can be obtained by measuring the shift of the trough in the MZI spectrum and the shift of the centroid in the SPR signal, respectively. Therefore, temperature compensation can be achieved.

3.4. Glucose measurement

As mentioned above, the sensor detected changes in the RI on the surface of the optical fiber to determine the concentration of glucose while performing temperature compensation to reduce the temperature crosstalk. This method was used attaching a PBA to the surface of the sensor to measure its response to glucose concentration. The sensor was functionalized by immersing it in a PBA dissolved in acetonitrile for 4 h to create the required interaction between the PBA and the rGO attached

to the sensor surface. Then, at a constant temperature of 30 °C, the sensor was successively immersed in glucose solutions (purchased from Merck, Germany) with concentrations of 0, 1, 2.5, 5, 7.5, 10, 12.5, 15 and 20 mmol/L for testing, which covered the normal sugar content in the human blood which ranges from 3.9 to 6.1 mmol/L. After the spectrum stabilized for about 60 s, the transmission spectrum was recorded and the remaining glucose on the sensor surface was washed off with deionized water until the transmission spectrum returned to its initial state. Each concentration was tested thrice and the average value was used for the subsequent analysis.

The normalized SPR and MZI spectra obtained by FFT demodulation of the original spectrum are shown in Fig. 11(a) and 11 (b), respectively. As expected, the dielectric constant of the sensing film changes upon binding with the glucose molecules, resulting in red shifts in both spectra. As the glucose concentration increases, the SPR resonance and MZI wavelength shifted by 33.2 nm and 2.36 nm, respectively, as shown in Fig. 11(c). It can be observed from the Fig. 11(c) that the sensor's sensitivity diminishes as the glucose concentration rises. This pattern could possibly be attributed to the saturation of the bonding activity between PBA and glucose molecules, which indeed inhibits subsequent binding reactions. In the 0–10 mM range, PBA can bind sufficiently with glucose molecules, resulting in good linearity. However, as mentioned above, the binding between PBA and glucose molecules is a dynamic adsorption process. When the concentration exceeds 10 mM, a fixed amount of PBA cannot fully absorb the glucose molecules, leading to a gradual stabilization of the redshift. It reaches saturation when the concentration exceeds 20 mM. Therefore, the sensor exhibits good linearity within 10 mmol and has a maximum detection limit of 20 mM, making it suitable for detecting low-concentration glucose solutions. As per the data represented in Fig. 11(d), the sensitivities of the SPR and MZI are 2.656 nm/mM and 0.1608 nm/mM, correspondingly, within a concentration range of 0 to 10 mM/L. To enhance the accuracy of the sensor, we used the centroid-fitting method to process the SPR spectrum and obtain the centroid coordinates of the region bounded by the baseline and SPR curves. The optimized linear fitting diagram, shown in Fig. 11(e), demonstrates higher linearity, with a sensitivity of 2.819 nm/mM and R-square of 0.991. It can be observed that the linearity of the sensor improved from 0.97477 to 0.991 after the fitting optimization, indicating that the sensor has a higher level of accuracy. Additionally, because glucose and deionized water share similar thermo-optical coefficients [35], we performed temperature compensation to account for the effect of temperature changes on glucose. The sensitivity matrix expressed by the following equation was used to obtain accurate and reliable readings, as demonstrated by our results.

$$\begin{bmatrix} \Delta\lambda_{SPR} \\ \Delta\lambda_{MZI} \end{bmatrix} = \begin{bmatrix} s_c^{SPR} & s_T^{SPR} \\ s_c^{MZI} & s_T^{MZI} \end{bmatrix} \begin{bmatrix} \Delta c \\ \Delta T \end{bmatrix} \quad (13)$$

Inserting experimental data into Eq. (11), Δn and ΔT can be represented by the following matrix:

$$\begin{bmatrix} \Delta c \\ \Delta T \end{bmatrix} = \begin{bmatrix} 2.819 & -0.12 \\ 0.1608 & 0.331 \end{bmatrix}^{-1} \begin{bmatrix} \Delta\lambda_{SPR} \\ \Delta\lambda_{MZI} \end{bmatrix} \quad (14)$$

$\Delta\lambda_{SPR}$ and $\Delta\lambda_{MZI}$ represent the wavelength shifts of the SPR centroid and MZI interference fringe, respectively. s_c^{SPR} and s_c^{MZI} are the glucose solution concentrations sensitivities of the SPR and MZI signals, respectively, while s_T^{SPR} and s_T^{MZI} represent the temperature sensitivities of the SPR and MZI signals, respectively. Δc and ΔT represent the changes in the glucose solution concentrations and temperature detected by the sensor, respectively. These results highlight the significance of optimization for improving the accuracy and reliability of glucose measurements. Before optimization, the SPR spectrum underwent a blue shift with temperature change, exhibiting poor linearity which leads to inaccurate glucose measurements. However, the optimized spectrum exhibited higher linearity, and sensitivity, highlighting the importance of optimization in obtaining accurate and reliable readings. To verify the

temperature compensation characteristics of the sensor, the sensor was immersed in glucose solutions of 1 mmol, 2.5 mmol, and 5 mmol respectively, and the temperature of the solution was increased from 30 °C degrees to 40 °C degrees, recording the spectral offset every 2 degrees. As can be seen from Fig. 11(f), after temperature compensation, the sensor is almost unaffected by external temperature interference, proving that the sensor has good temperature stability.

Additionally, to verify the potential impact of various substances such as cholesterol, potassium chloride, sodium chloride, sucrose, and other molecules present in the blood on the performance of the sensor, we conducted their selective testing. The sensor's specificity was investigated by detecting typical high-concentration substances, sucrose, sodium chloride, potassium chloride, and cholesterol, at the same concentration of 5 mM, typical for human blood. The results shown in Fig. 12 indicate that the maximum dip wavelength shift for the glucose solution is 17 nm, which is significantly greater than that of the sample with the other substances. Due to the specific absorption of PBA, the selectivity of the sensor towards glucose molecules is superior to the interferents (cholesterol, sucrose, KCl, NaCl). However, the influence of other substances can be taken into account. Considering that the spectral shift caused by other substances is due to the adsorption of these substances by rGO, and PBA cannot form covalent bonds with these substances, one can introduce a reference sensor of the same design but without PBA which will have different sensitivities to glucose and an interferent. Measuring the spectral shifts for both sensors and knowing their calibrated sensitivities for both substances, one can extract concentration of glucose even in the presence of the interferent. In order to conduct repeatability tests, 3 glucose sensors were used to detect a glucose concentration of 2 mM. The recorded normalized SPR spectra are shown in Fig. 12(b). The almost overlapping curves indicate that, under the same glucose concentration, the three sensors have the same SPR spectra and the resonance wavelength, demonstrating that the prepared probes have good repeatability. The long-term stability of the sensor is also an important indicator, as factors like oxidation of the metal layer can cause drift or deterioration in sensor performance. Therefore, we conducted stability testing on the sensor. As shown in Fig. 12(c), the sensor was subjected to three measurements per day in a 1 mM glucose solution for 14 days, and the average value was taken. The centroid position of each signal was recorded to determine the stability of the sensor. It can be seen from the Fig. 12(c) that the centroid coordinates are almost the same, with a standard deviation (SD) of 0.112. This indicates that the sensor exhibits good stability. Furthermore, we can calculate the limit of detection (LOD) as 0.12 mmol/L using the formula defined as three times the standard deviation multiplied by the reciprocal of the sensitivity.

Table 1 presents a comparison of optical sensors of various types with the one proposed in this study. According to Table 1, compared to the Side-polished flexible SPR and MMF without Cladding sensor, the proposed sensor has better sensitivity together with temperature compensation, thereby significantly improving the detection accuracy. The proposed sensor's sensitivity may not match glucose oxidase-enhanced dual-channel SPR fiber sensors or Au nanoparticle-equipped sensors, but it has a superior detection limit, amplified by rGO surface modification which could effectively adsorb PBA to increase the upper detection limit of the sensor. Unlike the glucose oxidase method, PBA has better accuracy because its absorption efficiency of glucose is less disturbed by external temperature. Compared to enzyme electrodes, fluorescence, and radio frequency methods, the SPR optical fiber sensor has an advantage of simple structure, minimal temperature effects, and strong electromagnetic resistance.

With the development of SPR and two-dimensional material technology, optical fiber sensors have achieved significant progress in the field of bio-sensing, such as detecting the novel coronavirus, human blood glucose, histamine, collagen, and other biomolecules [38–45]. However, despite the fact that the proposed optical fiber sensor has shown various advantages, the problem of high dependence on the

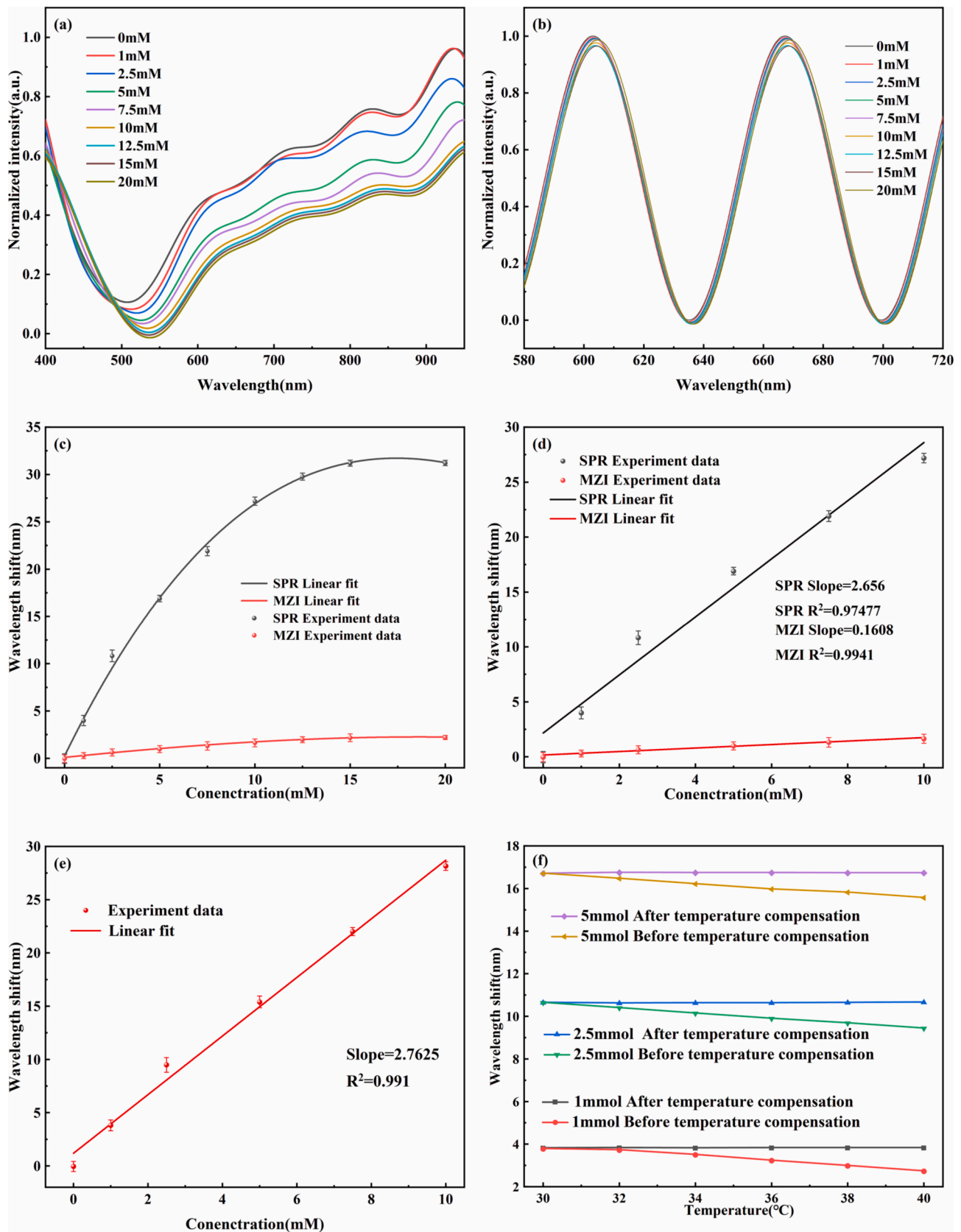


Fig. 11. Experimental data of the sensor in the range 0–10 mM at 30 °C for (a) SPR signals (b) MZI signals. (c) Wavelength shift and (d) linear part of wavelength shift (e) optimized linear fit of SPR signals. (f)The temperature compensation test of the sensor.

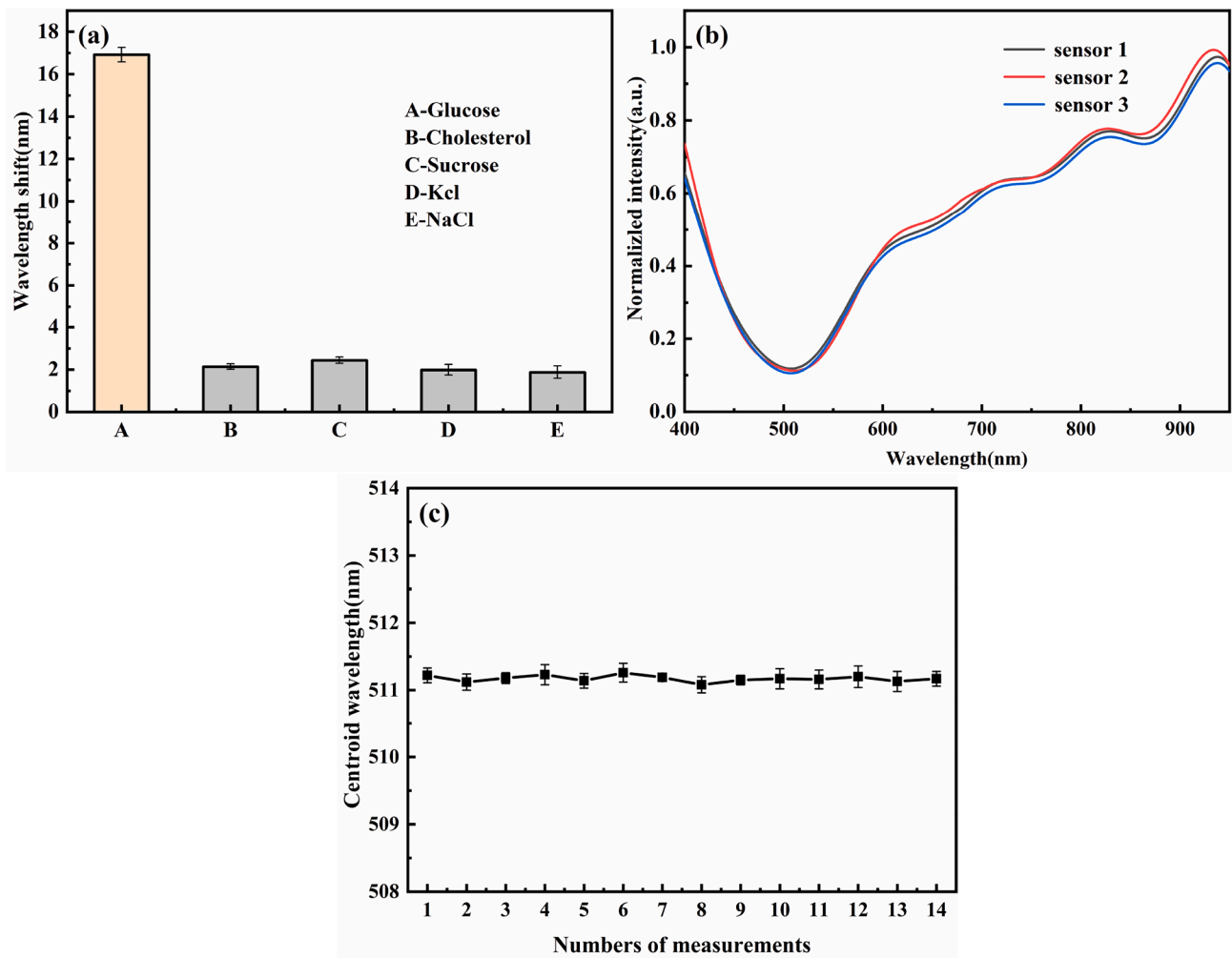


Fig. 12. (a) Specificity, (b) reproducibility and (c) stability test of the sensor.

Table 1

Comparison with the Performance of Glucose Sensors Reported Previously.

| Techniques | Glucose Concentration Sensitivity | Temperature compensation | Linear Range | Reference |
|---|-----------------------------------|--------------------------|--------------|-----------|
| SPR sensor with modified Au nanoparticles | 1.647 nm/mM | No | 0–5 mM | [3] |
| D-shaped flexible SPR sensor | 1.944 nm/mM | No | 0–10 mM | [36] |
| MMF without Cladding | 2.25 nm/mM | No | 0–8 mM | [37] |
| Dual-channel SPR fiber sensor | 6.156 nm/mM | Yes | 0–1.5 mM | [5] |
| Tapered SMF | 2.789 nm/mM | Yes | 0–10 mM | This work |

spectrometer and light source makes it difficult to integrate it into various medical devices. The problem limiting the possibility of miniaturization can be addressed by introducing a miniaturized light source and integrating the fiber-optic sensor with chip-level spectrometers. By using a microcontroller, the transmitted optical signal can be converted to an electrical signal, which communicates wirelessly with the host computer via methods like WiFi. Incorporating machine learning to analyze the transmitted spectral signals ensures accurate detection of blood glucose concentration. This is a problem that needs to be addressed in the follow-up of this article.

4. Conclusion

In summary, this study presents an innovative sensor design that combines the MZI and SPR effects to simultaneously detect glucose concentration and solution temperature to perform temperature compensation. The use of the FFT enabled the separation of the MZI and the SPR effects, while the proposed centroid-fitting algorithm effectively improved the linearity and linear detection range of the sensor. Furthermore, the proposed sensor was tested to detect glucose concentration. After centroid fitting and temperature compensation optimization, the sensor demonstrated high sensitivity, low susceptibility to the external temperature, high accuracy, low production cost, and ease of manufacturing. These features make it suitable for various biological analysis fields that require the detection of glucose concentration. Overall, the results of this study demonstrate the significant potential of the proposed sensor for various applications, such as monitoring human blood glucose levels, medical diagnosis, and environmental monitoring. These findings provide valuable insights into the design and optimization of sensitive and accurate glucose sensors, which could potentially lead to the development of novel and improved fluid analysis technologies.

Funding

National Natural Science Foundation of China (62175114).

Declaration of Competing Interest

The authors declare that they have no known competing financial interests or personal relationships that could have appeared to influence the work reported in this paper.

Data availability

Data will be made available on request.

References

- Z.V. Lee, E.J. Llanes, R. Sukmawan, N. Thongtang, H.Q.T. Ho, P. Barter, R. P. i. A. N. Cardiovascular, Prevalence of plasma lipid disorders with an emphasis on LDL cholesterol in selected countries in the Asia-Pacific region, *Lipids in Health and Disease* 20 (2021) 33.
- T. Pillinger, K. Beck, C. Gobjila, J.G. Donocik, S. Jauhar, O.D. Howes, Impaired Glucose Homeostasis in First-Episode Schizophrenia: A Systematic Review and Meta-analysis, *JAMA Psychiat.* 74 (3) (2017) 261–269.
- Z. Chen, F. Zhang, Y. Li, J. Shan, Y. Lu, Q. Liu, Bio-electron transfer modulated localized surface plasmon resonance biosensing with charge density monitoring, *Biosens. Bioelectron.* 201 (2022), 113956.
- H. Xu, X. Yang, G. Li, C. Zhao, X. Liao, Green synthesis of fluorescent carbon dots for selective detection of tartrazine in food samples, *J. Agricult. Food Chem.* 63 (2015) 6707–6714.
- W.L. Zheng, Y.N. Zhang, L.K. Li, X.G. Li, Y. Zhao, A plug-and-play optical fiber SPR sensor for simultaneous measurement of glucose and cholesterol concentrations, *Biosens. Bioelectron.* 198 (2022), 113798.
- S. Wu, Q. Tan, E. Forsberg, S. Hu, S. He, In-situ dual-channel surface plasmon resonance fiber sensor for temperature-compensated detection of glucose concentration, *Opt. Express* 28 (2020) 21046–21061.
- Y. Liu, X. Li, Y.-N. Zhang, Y. Zhao, Fiber-optic sensors based on Vernier effect, *Measurement* 167 (2021) 108451.
- V. Semwal, B.D. Gupta, “Highly selective SPR based fiber optic sensor for the detection of hydrogen peroxide,” *Sens. Actuators, B* 329 (2021) 129062.
- Y. Liu, W. Peng, Fiber-Optic Surface Plasmon Resonance Sensors and Biochemical Applications: A Review, *J. Lightwave Technol.* 39 (12) (2021) 3781–3791.
- Z. Pu, R. Wang, J. Wu, H. Yu, K. Xu, D. Li, “A flexible electrochemical glucose sensor with composite nanostructured surface of the working electrode,” *Sens. Actuators, B* 230 (2016) 801–809.
- B.A. Prabowo, A. Purwidyantri, K.-C. Liu, Surface plasmon resonance optical sensor: A review on light source technology, *Biosensors* 8 (2018) 80.
- B. Li, X. Yan, X. Zhang, F. Wang, S. Li, T. Suzuki, Y. Ohishi, T. Cheng, No-core optical fiber sensor based on surface plasmon resonance for glucose solution concentration and temperature measurement, *Opt. Express* 29 (2021) 12930–12940.
- R. Wang, H. Zhang, Q. Liu, F. Liu, X. Han, X. Liu, K. Li, G. Xiao, J. Albert, X. Lu, T. Guo, Operando monitoring of ion activities in aqueous batteries with plasmonic fiber-optic sensors, *Nat. Commun.* 13 (2022) 547.
- S. Chen, Y. Liu, Q. Liu, W. Peng, Temperature-Compensating Fiber-Optic Surface Plasmon Resonance Biosensor, *IEEE Photon. Technol. Lett.* 28 (2016) 213–216.
- S. Zeng, K.V. Sreekanth, J. Shang, T. Yu, C.K. Chen, F. Yin, D. Baillargeat, P. Coquet, H.P. Ho, A.V. Kabashin, Graphene–gold metasurface architectures for ultrasensitive plasmonic biosensing, *Adv. Mater.* 27 (2015) 6163–6169.
- M. Pisco, F. Galeotti, G. Quero, G. Grisci, A. Micco, L.V. Mercedo, P.D. Veneri, A. Cutolo, A. Cusano, Nanosphere lithography for optical fiber tip nanoprobe, *Light Sci. Appl.* 6 (5) (2017) e16229.
- H. Song, Q. Wang, W.-M. Zhao, A novel SPR sensor sensitivity-enhancing method for immunoassay by inserting MoS₂ nanosheets between metal film and fiber, *Opt. Laser Eng.* 132 (2020), 106135.
- Q. Wang, B. Wang, Sensitivity enhanced SPR immunosensor based on graphene oxide and SPA co-modified photonic crystal fiber, *Opt. Laser Technol.* 107 (2018) 210–215.
- M. Li, R. Singh, C. Marques, B. Zhang, S. Kumar, 2D material assisted SMF-MCF-MMF-SMF based LSPR sensor for creatinine detection, *Opt. Express* 29 (2021) 38150–38167.
- G. Eda, G. Fanchini, M. Chhowalla, Large-area ultrathin films of reduced graphene oxide as a transparent and flexible electronic material, *Nat. Nanotechnol.* 3 (2008) 270–274.
- R. Kant, R. Tabassum, B.D. Gupta, Integrating nanohybrid membranes of reduced graphene oxide: chitosan: silica sol gel with fiber optic SPR for caffeine detection, *Nanotechnology* 28 (2017), 195502.
- V. Semwal, B.D. Gupta, “Highly sensitive surface plasmon resonance based fiber optic pH sensor utilizing rGO-Pani nanocomposite prepared by in situ method,” *Sens. Actuators, B* 283 (2019) 632–642.
- W. Liu, Z. Liu, Y.u. Zhang, S. Li, Y. Zhang, X. Yang, J. Zhang, L. Yuan, Specialty optical fibers and 2D materials for sensitivity enhancement of fiber optic SPR sensors: A review, *Opt. Laser Technol.* 152 (2022) 108167.
- A.B. Socorro, I. Del Villar, J.M. Corres, F.J. Arregui, I.R. Matias, Spectral width reduction in lossy mode resonance-based sensors by means of tapered optical fibre structures, *Sens. Actuators, B* 200 (2014) 53–60.
- A. Chopra, G.C. Mohanta, B. Das, R. Bhatnagar, S.S. Pal, Tuning the Sensitivity of a Fiber-Optic Plasmonic Sensor: An Interplay Among Gold Thickness, Tapering Ratio and Surface Roughness, *IEEE Sens. J.* 21 (2021) 12153–12161.
- T. Liu, H. Ding, C. Zhan, J. Huang, S. Wang, Simply and cost-effectively fabricated AuNP-based fusion spliced transmissive optical fiber LSPR probes, *Opt. Express* 29 (2021) 7398–7409.
- L. Li, Y.-N. Zhang, Fiber-optic SPR pH sensor based on MMF–NCF–MMF structure and self-assembled nanofilm, *IEEE Trans. Instrum. Meas.* 70 (2020) 1–9.
- X. Chen, X. Li, D. Yi, X. Hong, Y. Chen, Plasmonic tapered-fiber interference sensor for simultaneously detecting refractive index and temperature, *Opt. Lett.* 46 (2021) 6071–6074.
- Y.M. Kamil, M.A. Bakar, M. Mustapa, M. Yaacob, A. Syahir, M. Mahdi, Sensitive and specific protein sensing using single-mode tapered fiber immobilized with biorecognition molecules, *IEEE Photon. J.* 7 (2015) 1–9.
- Y. Xu, H. Bai, G. Lu, C. Li, G. Shi, Flexible graphene films via the filtration of water-soluble noncovalent functionalized graphene sheets, *J. Am. Chem. Soc.* 130 (2008) 5856–5857.
- X. Li, S.C. Warren-Smith, L. Xie, H. Ebendorff-Heidepriem, L.V. Nguyen, Temperature-compensated refractive index measurement using a dual Fabry-Perot interferometer based on C-fiber cavity, *IEEE Sens. J.* 20 (2020) 6408–6413.
- J.-M. Hsu, C.-L. Lee, P.-J. Huang, C.-H. Hung, P.-Y. Tai, Temperature sensor with enhanced sensitivity based on photonic crystal fiber interferometer with material overlay, *IEEE Photon. Technol. Lett.* 24 (2012) 1761–1764.
- Y. Jin, L. Zhou, J. Liang, J. Zhu, Electrochemically driven dynamic plasmonics, *Adv. Photonics* 3 (2021) 044002.
- K.M. Aly, E. Esmail, Refractive index of salt water: effect of temperature, *Opt. Mater.* 2 (1993) 195–199.
- P.R. Prasad, S.K. Selvaraja, M. Varma, Real-time compensation of errors in refractive index shift measurements of microring sensors using thermo-optic coefficients, *Opt. Express* 26 (2018) 13461–13473.
- H. Yu, Y. Chong, P. Zhang, J. Ma, D. Li, A D-shaped fiber SPR sensor with a composite nanostructure of MoS₂-graphene for glucose detection, *Talanta* 219 (2020) 121324.
- Y. Yuan, X. Yang, D. Gong, F. Liu, W. Hu, W. Cai, J. Huang, M. Yang, Investigation for terminal reflection optical fiber SPR glucose sensor and glucose sensitive membrane with immobilized GODs, *Opt. Express* 25 (2017) 3884–3898.
- G. Zhu, L. Singh, Y. Wang, R. Singh, B. Zhang, F. Liu, B.K. Kaushik, S. Kumar, Tapered Optical Fiber-Based LSPR Biosensor for Ascorbic Acid Detection, *Photonics Sens.* 11 (2020) 418–434.
- W. Zhang, R. Singh, Z. Wang, G. Li, Y. Xie, R. Jha, C. Marques, B. Zhang, S. Kumar, Humanoid shaped optical fiber plasmon biosensor functionalized with graphene oxide/multi-walled carbon nanotubes for histamine detection, *Opt. Express* 31 (2023).
- R. Singh, Z. Wang, C. Marques, R. Min, B. Zhang, S. Kumar, Alanine aminotransferase detection using TIT assisted four tapered fiber structure-based LSPR sensor: From healthcare to marine life, *Biosens. Bioelectron.* 236 (2023) 115424.
- L. Singh, R. Singh, B. Zhang, B.K. Kaushik, S. Kumar, Localized Surface Plasmon Resonance Based Hetero-Core Optical Fiber Sensor Structure for the Detection of L-Cysteine, *IEEE Trans. Nanotechnol.* 19 (2020) 201–208.
- P.S. Pandey, S.K. Raghuvanshi, A. Shadab, M.T.I. Ansari, U.K. Tiwari, S. Kumar, SPR Based Biosensing Chip for COVID-19 Diagnosis—A Review, *IEEE Sens. J.* 22 (2022) 13800–13810.
- G. Li, Q. Xu, R. Singh, W. Zhang, C. Marques, Y. Xie, B. Zhang, S. Kumar, Graphene Oxide/Multiwalled Carbon Nanotubes Assisted Serial Quadruple Tapered Structure-Based LSPR Sensor for Glucose Detection, *IEEE Sens. J.* 22 (2022) 16904–16911.
- B.K. Kaushik, L. Singh, R. Singh, G. Zhu, B. Zhang, Q. Wang, S. Kumar, Detection of Collagen-IV Using Highly Reflective Metal Nanoparticles—Immobilized Photosensitive Optical Fiber-Based MZI Structure, *IEEE Trans. NanoBiosci.* 19 (2020) 477–484.
- V.S. Chaudhary, D. Kumar, S. Kumar, SPR-Assisted Photonic Crystal Fiber-Based Dual-Wavelength Single Polarizing Filter With Improved Performance, *IEEE t. Plasma Sci.* 49 (2021) 3803–3810.